VTT Technical Research Centre of Finland

Hybrid films from cellulose nanomaterials—properties and defined optical patterns

Leppänen, Ilona; Hokkanen, Ari; Österberg, Monika; Vähä-Nissi, Mika; Harlin, Ali; Orelma, Hannes

ORIGINAL RESEARCH

Hybrid films from cellulose nanomaterials—properties and defined optical patterns

Ilona Leppänen · **Ari Hokkanen** ·
Monika Österberg · **Mika Vähä-Nissi** · **Ali Harlin** ·
Hannes Orelma

Abstract Polymer composites with nanocellulose as the reinforcing agent often lack good compatibility between the two components. In this study, we have combined cellulose nanofibrils (CNFs) and cellulose nanocrystals (CNCs) in different ratios to create all-cellulose films consisting of entirely discrete nanocellulose objects that complement each other. Then further, by applying the controlled dissolution concept we were able to create defined optical patterns on the films. The films consisting of 50% CNCs showed equivalent mechanical and barrier properties when compared to the pure CNF film. In addition, the incorporation of CNCs enabled tuning of the films' optical properties. To modify this film further, we prepared specific patterns on the film by controlled dissolution by impregnating the films with *N*-methylmorpholine-*N*-oxide (NMMO) followed by heat treatment and pressure. Mechanical testing and optical measurements of the patterned films showed the effect of the dissolved cellulose regions on the film properties. The controlled dissolution of the films increased the tensile strength of the films, however, the strain was decreased quite significantly. Altogether, the CNF/CNC hybrid films combine both nanomaterials' good properties. Cellulose nanofibrils have film-forming ability and incorporation of CNCs can further tune the optical, mechanical, and barrier properties, to optimize the films for varying applications such as optical sensors and packaging materials.

I. Leppänen (✉) · M. Vähä-Nissi · A. Harlin · H. Orelma
Biomass Processing and Products, VTT Technical
Research Centre of Finland Ltd., 02044 Espoo, Finland
e-mail: ilona.leppanen@vtt.fi

A. Hokkanen
Microelectronics, VTT Technical Research Centre
of Finland Ltd., 02044 Espoo, Finland

M. Österberg
Department of Bioproducts and Biosystems, School
of Chemical Engineering, Aalto University, Espoo, Finland

Graphical abstract
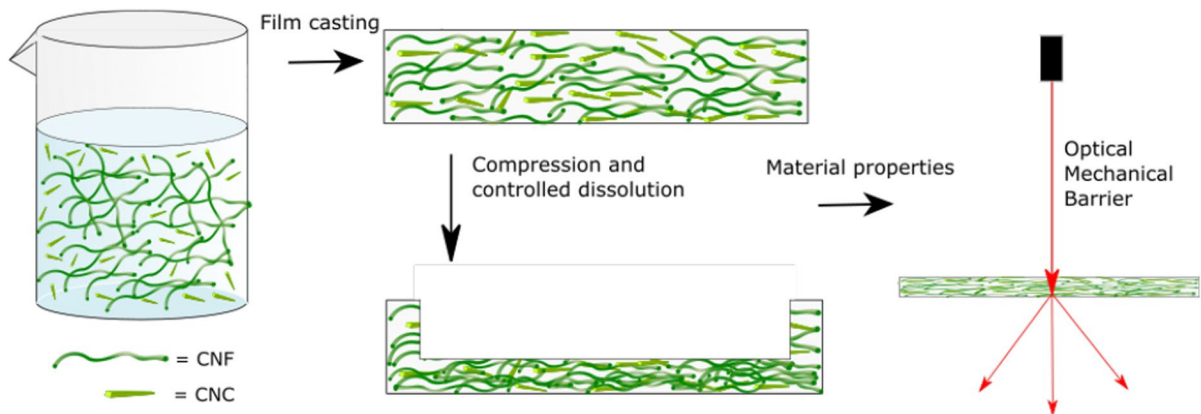
Introduction

There is an increasing demand for products made from renewable, non-petroleum based resources and consumers' awareness towards environmental concerns has pushed industries to seek for new "greener" solutions with lower environmental impact (Sathre and Gustavsson 2009) . One already utilized greener solution is cellulose, which is one of the most abundant biopolymers found in nature. It can be found for example in wood, where it functions as the primary component of the cell wall together with hemicellulose and lignin. Due to its outstanding properties, such as high availability, renewability, low cost, biodegradability and broad chemical modifying capacity, it has recently attained interest within both the scientific and industrial community as a means to reduce the use of non-renewable synthetic plastic materials. (Klemm et al. 1998, 2005) Owing to the hierarchical structure of the plant cell wall, nanosized components can be extracted from it. Nanocellulose is commonly classified as cellulose nanofibers (CNFs) and cellulose nanocrystals (CNCs). CNFs are long and thread-like filaments with high aspect ratio (length to width ratio) and both crystalline and disordered regions. CNFs are prepared mainly by mechanical disintegration of cellulosic fibers (Klemm et al. 2011). CNCs

on the contrary are short and rod-like nanomaterials. They are prepared by acid hydrolysis, where the disordered regions are removed and the crystalline proportion remains. Depending on the acid used, different functionalities are introduced on the CNC surface. CNC suspensions are known to form liquid crystal chiral nematic ordered structures above a critical concentration (Revol et al. 1992) and birefringent gels at even higher concentrations (Liu et al. 2011; Ureña-Benavides et al. 2011; Shafiei-Sabet et al. 2012; Shafeiei-Sabet et al. 2013), which make their rheological behavior very different from CNFs and also induce interesting optical properties. In materials research, both CNFs and CNCs have found applications in films (Siró and Plackett 2010; Lee et al. 2014; Hubbe et al. 2017), foams (Lavoine and Bergström 2017), gels (De France et al. 2017) and filaments (Lundahl et al. 2017).

Composite technology sees nanocellulose as a promising material for future bio-based and biodegradable composites that involves a continuous polymer matrix and nanocellulose as the reinforcing agent. However, this is not easily achieved since common polymer matrices are often hydrophobic and thus not compatible with cellulose. This has raised interest in all-cellulose composites (Nishino et al. 2004; Zhao et al. 2014; Li et al. 2018), which are cellulose-based composites usually made from regenerated cellulose as the polymer matrix and nanocellulose fibers (Yang et al. 2015) or crystals (Ma et al. 2011) as the reinforcing agent. Another approach is

partial dissolution, which dissolves the surface of the cellulose fibers leaving the inner part intact (Chen et al. 2020; Orelma et al. 2017). By combining two chemically similar cellulosic substances the composite obtains good interfacial compatibility, biocompatibility, and biodegradability (Nishino et al. 2004; Li et al. 2018). Strong hydrogen bonding between the components improves interfacial interaction, which ensures better adhesion and effective transfer of stress between the components. In addition to mechanical properties, good interfacial compatibility influences the optical and barrier properties of the composite films. Good oxygen barrier properties have been previously reported for 100% CNF films (Syverud and Stenius 2009; Aulin et al. 2010; Österberg et al. 2013) and for composite films containing CNFs (Plackett et al. 2010; Hansen et al. 2012; Yang et al. 2015) or CNCs (Saxena et al. 2010) as the reinforcing agent, among others. However, only few publications have been reported on the barrier properties of 100% CNC films (Belbekhouche et al. 2011; Herrera et al. 2014).

In this study, we have not only combined CNFs and CNCs to form hybrid films consisting of entirely discrete nanocellulose objects but also applied the controlled dissolution concept to incorporate partially dissolved regions within the film in defined patterns. Firstly, we have investigated the effect of CNC addition on the film properties to find the most interesting consistency. The film with 50% cellulose nanocrystals was shown to have comparable mechanical and barrier properties with the pure CNF film and the incorporation of CNCs to the film enabled decreasing of the light scattering. We were able to further tune the film properties, i.e. enhance tensile strength and modify optical properties, by applying the controlled dissolution process.

Experimental

Materials

Cellulose nanocrystals (CNCs) (spray-dried powder) were purchased from CelluForce, Quebec, Canada. The CNCs were prepared by sulfuric acid hydrolysis with a sulfate content of 246–261 mmol kg^{-1}. We measured the length and width of the Celluforce CNCs from AFM images and the distributions are presented in Supplementary Information (Suppl.

Fig. S1). The average width was 3.85 nm and the length 140 nm. The values are in the range or close to the values reported by the supplier (diameter of 2.3–4.5 nm and length of 44–108 nm). This indicates that the crystals were properly dispersed. Cellulose nanofibrils (CNFs) were obtained by processing bleached Finnish hardwood (birch) pulp (Metsä Fibre, Finland) with a carbohydrate content of 73 wt% glucose, 23 wt% xylose, and 0.15 wt% methyl glucoronic acid. The pulp suspension was first processed through a Masuko grinder (Supermasscolloider MKZA10-15 J, Masuko Sangyo Co., Japan) with two passes with subsequent fluidization with six passes by a high pressure microfluidizer (Microfluidics Corp. Newton, MA, USA). The microfluidizer was equipped with two Z-type chambers that had diameters of 400 μm and 100 μm and it operated at 2000 bar pressure. The final consistency of the CNF suspension was 1.68 wt%. 4-Methylmorholine-*N*-Oxide monohydrate (NMMO) ($\geq 95.0\%$ (N)) was ordered from Sigma. All other chemicals used in this study were of analytical grade and used as received.

Film preparation

A 6 wt% cellulose nanocrystal suspension was prepared by adding the spray-dried CNC powder to water through a sieve and mixing simultaneously with a magnetic stirrer. Once all CNC powder was

Table 1 Solid contents and compositions of the CNF/CNC hybrid films

Sample	Dispersion solids content (wt%)	CNF wt% in film	CNC wt% in film	Sorbitol wt% in film
CNF100	1.68	100	0	0
CNF75CNC25	2.05	75	25	0
CNF50CNC50	2.63	50	50	0
CNF25CNC75	3.65	25	75	0
CNC100	6	0	100	0
CNF100+s	2.16	77	0	23
CNF-75CNC25+s	2.63	58	19	23
CNF-50CNC50+s	3.37	38.5	38.5	23
CNF-25CNC75+s	4.65	19	58	23
CNC100+s	7.53	0	77	23

added, the suspension was ultra-sonicated (400 W tip sonicator, Branson 450 Digital Sonifier, Branson Ultrasonics, Danbury, USA) for 3 min with 40% amplitude and left to mix for 48 h using a magnetic stirrer. After mixing the suspension was ultra-sonicated again 4×6 min with 40% amplitude to eliminate any remaining aggregates. Different CNF to CNC dry weight ratio suspensions (CNF100, CNF-75CNC25, CNF50CNC50, CNF25CNC75, CNC100) were prepared by mixing targeted amounts of CNC (6 wt%) and CNF (1.68 wt%) suspensions in a speed mixer (DAC 1100.1 VAC-P, Synergy Devices Limited, High Wycombe, UK). Films were prepared with and without addition of sorbitol (s), which acted as an external plasticizer for the hybrid films. Suspensions to which sorbitol was added contained 30% of sorbitol with respect to the amount of dry CNFs+CNCs. The relative compositions of the films are presented in Table 1.

All suspension except CNC100 and CNC100+s were solvent casted on a polypropylene substrate, which was plasma-treated (100%) to enhance the adhesion of CNF/CNC mixtures on the substrate. CNC100 and CNC100+s were cast on Petri dishes since the dispersion was not viscous enough to spread evenly on the substrate. The CNF/CNC films were dried in room temperature (RT) and stored in 23 °C and 50% relative humidity (RH).

Rheology of the CNF/CNC suspensions

The steady-state shear viscosity of the different samples was measured using a rotational rheometer (Anton Paar Rheometer MCR301) with a four-bladed vane geometry (ST22-4 V-40), which was brought down into a cylindrical measuring cup holding the sample. A 1 mm gap was used. Measurements were performed in RT. The viscosity was measured between shear rates 0.1 s^{-1} and 1000 s^{-1}.

Fourier transform infrared spectroscopy (FT-IR)

FT-IR measurements were carried out using a Thermo Scientific Nicolet iS50 FT-IR spectrometer equipped with an ATR diamond (Thermo Scientific, USA) to identify any changes related to the different weight ratios of CNFs to CNCs. All spectra were obtained from 32 scans with a resolution of 4 cm^{-1}

throughout the wavenumber range from 400 to 4000 cm^{-1}. Dry films were placed on the ATR crystal and the IR spectrum was measured. At least three repetitions per sample were conducted.

Atomic force microscopy (AFM)

The surface topography and morphology of the prepared films was investigated using Atomic Force Microscopy (AFM) to reveal the distribution of the two materials in the film. AFM imaging of the films surfaces was performed using a NanoTA AFM + instrument (Anasys Instruments, Bruker, MA, USA). The images were recorded in tapping mode in air with scan rate of 0.5 Hz using silicon cantilevers (Applied Nanostructures Inc., Santa Clara, CA, USA). The damping ratio was around 0.7–0.85 Hz. The films were attached onto steel supports with double-sided tape and for each sample, three different areas were scanned and the images were not processed by any other means except flattening.

Scanning electron microscopy (SEM) and energy-dispersive X-ray spectroscopy (EDS)

SEM and EDS were used to determine the visual structure of the films and detect the elemental sulfur originating from the sulfate groups on the CNCs, respectively. SEM imaging was carried out with a Merlin Field Emission FE-SEM (Carl Zeiss NTS GmbH, Germany), which was coupled with an EDS detector (Thermo Scientific UltraDry silicon drift X-ray detector). Ca. 1 cm^2, pieces were cut from the CNF/CNC films and attached on SEM sample holders that were coated with carbon tape. Film samples on the holders were subsequently coated with gold by sputtering (2 nm, ~30 s) to improve sample conductivity. All SEM images were imaged with the electron gun voltage of 2–5 kV and the grid current of 60 pA. The pixel resolution in the images was 2048×1536 pixels. Images were taken from approximately three different locations. The EDS data was collected with a 1000× magnification.

Mechanical properties

Tensile strength, Young's modulus, and strain at break of the films were measured by a Lloyd LS5 materials testing machine (AMETEK measurement

and calibration technologies, USA) at 23 °C and 50% RH with a load cell of 100 N. The samples were kept under these conditions at least overnight before the measurement. The initial grip distance was 30 mm and the rate of the grip separation 10 mm min^{-1}. The specimens were cut into 15 mm (original samples) or 5 mm (NMMO-treated and reference samples) wide strips with a lab film cutter. The 5 mm width was the width of one square formed in the patterning. Thus, the partially dissolved and non-dissolved areas alternated within the sample. Seven replicates of each sample were measured. Thicknesses of each specimen was measured separately with a digital caliber from three different points. The average thickness was used for the calculations.

Optical properties

The transparency of the CNF/CNC hybrid films was evaluated by measuring the transmittance using a Perkin Elmer Lambda 900 UV/VIS/NIR spectrometer (Perkin-Elmer, USA) equipped with a film holder. Transmittance of all films was measured by using wavelength range of 200–800 nm with 1 nm measurement resolution. At least three repetitions per sample were conducted.

Transmittance, forward/backward scattering and absorption of CNF/CNC cellulose films was analyzed with a red diode laser (659 nm and 1.3 mW). A single mode fiber with a 9 μm core and a 125 μm cladding diameter was coupled from the laser to a collimation lens F230FC-1550 from Thorlabs (Suppl. Fig. S2a). The collimated laser beam was aligned to the integrated sphere IS200-4 (Thorlabs) that has a polytetrafluoroethylene (PTFE) coating inside for light reflection. A multimode fiber with a 200 μm core and a 220 μm cladding diameter (Thorlabs) collected light from the integrated sphere to the fiber optic power meter (Fotec m). For transmittance and forward scattering measurements, the hybrid films were placed on the input port. The input port size was decreased with an aluminum plate having a 2.5 mm diameter hole to maximize the light collection. The output port was closed with a PTFE plug in the transmittance measurements and with a SMA connector that has a 3.2 mm diameter hole in the PTFE coating in the forward scattering measurements. In the backward scattering measurement, CNF/CNC films were placed in the output port and the output port size was decreased

to 2.5 mm with the aluminum plate hole. The input port size was decreased to 3.2 mm with the PTFE coated SMA connector.

Scattering angles were measured with the same red diode laser (Suppl. Fig. S2b). As the collimated laser beam hit the CNF/CNC films, the scattered light was measured from the screen with a mobile phone camera. Distance between the sample and the screen was 313 mm. The intensity distribution was defined from the picture and the scattered beam diameter was calculated with Gaussian beam width, where intensity has been dropped $1/e^2 \approx 0.135$ (Saleh and Teich 1991).

Barrier properties

Air permeances of the samples were tested using an L&W Air Permeance Tester. Measurements were repeated three times. *Oxygen transmission rates* (cm^3 m^{-2} d^{-1}) were measured with an OX-TRAN 2/22H Permeation Analyzer (AMETEK MOCON, USA) complying with several ASTM, DIN and ISO standards, such as modified ASTM F1927 (Standard Test Method for Determination of Oxygen Gas Transmission Rate, Permeability and Permeance at controlled Relative Humidity Through Barrier Materials Using a Coulometric Detector), which was applied here. Specimens with dimensions of 5 cm×5 cm were cut from the films. Thickness of each specimen was measured from nine different locations using a L&W Micrometer 51 (Lorentzen & Wettre, Sweden). Specimens were then masked on both sides with an adhesive backed aluminum foil providing a test area of 5 cm^2. Tests were carried out at 23 °C, and relative humidity of both the test and the carrier gas flows was set to 50%. Oxygen permeation (OP) values expressed as cm^3 μm m^{-2} d^{-1} kPa^{-1} are reported. Two to three specimens were tested for each film type. *Grease barrier properties* were investigated according to the method reported previously by Vähä-Nissi et al. (2016) This method was modified from ISO 16235-2 and combined with selected parts of TAPPI T507 cm-99. Blotting paper sheets were cut into the size of 5 cm×5 cm and placed on a transparent glass plate. The film samples (5 cm×5 cm) were arranged on top of the papers. A circular blotting paper was then placed on top of the sample and 200 μl of 0.5 wt% "Oil Red O" dyed olive oil was pipetted onto the circular blotting paper. Subsequently, a weight of 50 g

was placed on top of the blotting paper. Penetration of grease through the samples was detected by an image scanner. Four to five parallel samples were measured for 7 days with periodic image scanning. Images were taken more frequently on the first day and after that 2 times a day.

Preparation of defined macrosize optical structures by controlled dissolution using NMMO (N-methylmorpholine N-oxide)

CNF50CNC50 + s film was chosen for further studies to prepare a defined structure to the surface by controlled dissolution with NMMO. The dissolution was conducted as reported earlier by Orelma et al. (2017), with slight modifications in the heat activation step to create only locally dissolved and compressed areas. NMMO was dissolved in aqueous methanol (88 wt% methanol and 12 wt% water), with a NMMO consistency of 25 wt%. The CNF50CNC50 + s film was immersed in the NMMO solution for 2 h, and subsequently dried between blotting papers overnight. A reference sample was prepared by immersing the film in pure aqueous methanol without NMMO. The heat activation of the dried films was carried out using metal plates with patterning to partially dissolve certain areas of the films, creating defined structures (Suppl. Fig. S3). The metal plates were pressed against the NMMO doped films using a hydraulic press with temperature and pressure control (Lab Tech Engineering Company Ltd.). Three printer papers and cellophane were placed between the metal plate and the hybrid film. The papers ensured that the contact between the metal plate and sample was even and the cellophane ensured that the film did not stick to the papers. The heat was set to 130 °C and the pressure was approximately 2500 kg/cm^2. The films were kept under pressure and heat for 10 s after which they were regenerated in methanol for 1 + 1 h. The films were dried in room temperature and stored in 23 °C and 50% relative humidity (RH).

Solid state ^{13}C CP-MAS NMR

The ^{13}C cross polarization (CP) magic angle spinning (MAS) nuclear magnetic resonance (NMR) measurements were performed to detect changes in crystallinity after the controlled dissolution process. The NMR spectra was collected from the NMMO treated film from both the compressed area (area around the squares) and non-compressed area (square) and from an original CNF50CNC50 + s film. The measurements were performed using an Agilent DD2 600 NMR spectrometer with magnetic flux density of 14.1 T, equipped with a 3.2 mm T3 MAS NMR probe operating in a double resonance mode. The samples were packed in ZrO$_2$ rotors, and the MAS rate in the experiments was set to 10 kHz. 8000 scans were accumulated using a 1.3 ms contact time and a 6.0 s delay between successive scans. Protons were decoupled during acquisition using SPINAL-64 proton decoupling with a field strength of 80 kHz. 90° pulse durations and Hartmann-Hahn match for cross polarization were calibrated using α-glycine. The chemical shift scale was externally referenced to adamantane signal at 38.48 ppm. All processing was carried out using TopSpin 4.0 software.

Confocal microscopy

The surface roughness and quality of films were investigated after the controlled dissolution with an S Neox 3D Optical Profiler confocal microscopy (Sensofar Metrology, Spain) to identify differences between the partially dissolved and non-dissolved areas. EPI 5× and EPI 50× objectives were used in the analysis.

Results and discussion

Rheological behavior of suspensions

We studied the large deformation steady-state rheology of all the different CNF/CNC suspensions, with and without sorbitol (Fig. 1a, b). The concentrations of the suspensions varied from 1.68 wt% for pure CNFs to 7.53 wt% for pure CNCs with sorbitol. Even though the solid content for pure CNF suspensions was over three times lower than for pure CNC suspensions, the viscosities of the pure CNF suspensions were 10,000 times higher than that of pure CNCs both with and without sorbitol. The reason for this is that already at very low solids content CNFs form gel networks, where the nanofibrils interact strongly with each other due to their high aspect ratio (Pääkko et al. 2007). Due to the dominating effect of the fibrillar gel network small additions of CNCs did not affect
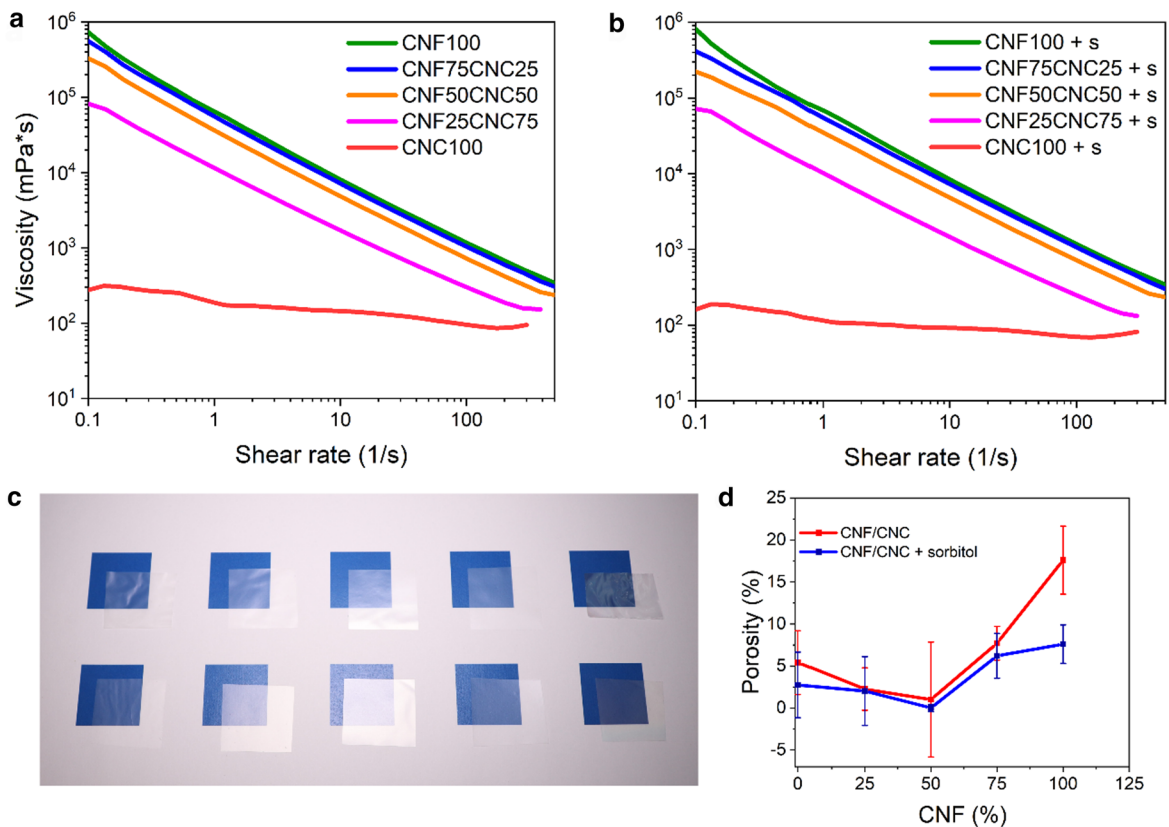
Fig. 1 Viscosity of CNF/CNC suspensions without sorbitol (**a**) and with sorbitol (**b**) as the function of shear rate. **c** Image of films: upper row without sorbitol and lower row with sorbi-tol starting from CNF100CNC0 to CNC100CNF0 from left to right. **d** Porosity of CNF/CNC hybrid films

the viscosity of the gel, only at 25% CNC content we could observe a clear decrease in viscosity. All the suspensions containing CNFs, both with and without sorbitol showed shear-thinning behavior, which is a characteristic feature of CNF suspensions. Thus, the trend of the shear viscosity curves for all the suspensions except the pure CNCs was very similar. Under shear, due to their rod-like morphology, CNCs naturally align along the shear direction, exhibiting three distinct regions, which is a typical rheological behavior for lyotropic liquid crystals (Onogi and Asada 1980; Shafiei-Sabet et al. 2012). First, there is a shear-thinning region, where the chiral nematic liquid crystal domains align, followed by a plateau region where all the domains have aligned along the shear direction. Finally, there is a second shear-thinning region at high shear rates where these domains are destroyed and the individual crystals align along the flow direction (Shafiei-Sabet et al. 2012). The

regions are more visible when the CNC viscosity profiles are presented independently, especially for the CNCs without sorbitol (Suppl. Fig. S4). This distinct behavior was not observed with the addition of 25% CNFs. The effect of sorbitol addition on the rheological properties of the suspensions was minor and the results correlated with previously reported results (Koppolu et al. 2018).

Hybrid film preparation

We cast the nanocellulose hybrid films from CNF/CNC suspensions (Table 1; Fig. 1c). From the processing point of view, there were many advantages in using mixtures of CNFs and CNCs as raw materials. CNCs appeared to have a positive effect on the film-forming ability during film preparation. The films prepared from CNF/CNC mixtures spread more easily on the substrate and showed

Fig. 2 ATR-FTIR spectra of all CNF/CNC hybrid films without sorbitol (**a**) and with sorbitol (**b**)
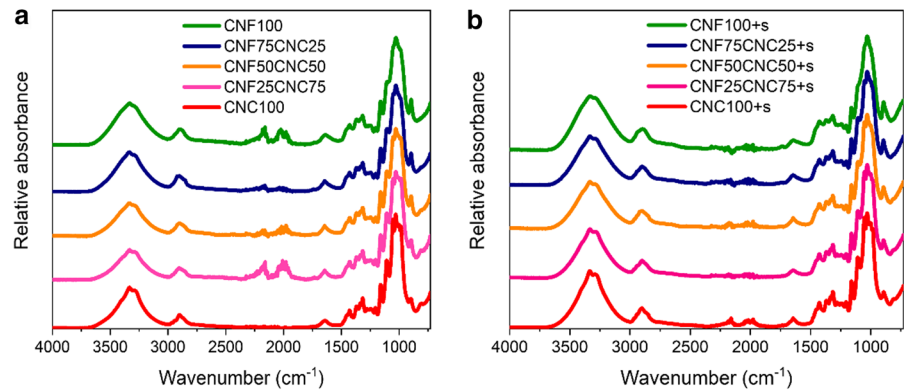
better adherence than the pure CNF films. Films with CNCs formed even films that showed only little (CNC content 25%) or no (CNC > 25%) shrinkage and wrinkling once the films were dried unlike the CNF100 film with no CNC or sorbitol. In general, addition of CNCs enhanced the processability of the CNF gel during film production. The conceivable reason is it's significantly lower viscosity compared to CNFs (Fig. 1a, b). Thus, a small addition of CNCs eases the application of the CNF gel in the nanocellulose film manufacturing. When water is evaporated during drying, the viscosity decreases more slowly allowing the structure to settle. This also prevents the formation of drying forces that tend to break the CNF films during their manufacturing. The film thicknesses varied slightly inside one film and the thicknesses for different measurements were always measured separately depending on where the sample was cut from the approximately A4 sized film. The porosities of the films were measured gravimetrically (Fig. 1d). The addition of CNCs decreased the porosity of the hybrid films in all tested concentrations. The lowest porosity was obtained with adding 50% of CNCs. Decreased porosity is a consequence of more efficient packaging of the short rod-like nanocrystals compared to the long nanofibrils. The CNCs are able to fill the voids within the CNF network, resulting in decreased porosity of the hybrid film. The plasticizer lowered the porosities of all tested films indicating easing of the formation of film structures. Decreasing porosity along with increasing CNC content is reported also for films made of TEMPO-CNFs and CNCs (Xu et al. 2016).

Chemical characterization with FTIR

Figure 2 presents the FTIR spectra of CNF/CNC hybrid films. As expected, they are very similar to each other with only minor differences. All samples exhibited the two main absorbance regions, 800–1500 cm^{-1} and 3000–3600 cm^{-1}, typical for cellulose I (Fan et al. 2012). The unique fingerprint area for cellulose I is in the region of 800–1500 cm^{-1}, and it can be found in all samples. The peak at 1150 cm^{-1} results from asymmetrical C–O–C stretching and the peaks closer to 1000 cm^{-1} from C–C, C–OH, C–H ring and side group vibrations. The broad band in the 3600–3000 cm^{-1} range is due to stretching vibrations of hydrogen bonded OH-groups (Fan et al. 2012). Cellulose binds water very tightly, which is why residual water is always present in cellulose samples. The peak at around 1630 cm^{-1} originates from this bound water and it also contributes to the intensity of the broad band at 3600–3000 cm^{-1}. Two minor peaks around 3300 cm^{-1} and 3200 cm^{-1}, which may be ascribed to intermolecular hydrogen bonding, can be identified for the films containing CNCs. These peaks are not as clear in the spectrum of the pure CNF film, which may be due to higher amount of intermolecular bonding between CNCs, as suggested by Xu et al. (2013). However, we note that bound water is also affecting this region and CNCs with higher negative charge may be leading to higher amount of bound water. The peak at around 2900 cm^{-1} originates from the symmetrical C–H stretching vibrations (Sun et al. 2015). For the samples containing CNCs, an additional peak can be observed at around 800 cm^{-1} corresponding to symmetric stretching of the sulfate ester linkages S–O–C (Chen et al. 2013). This peak
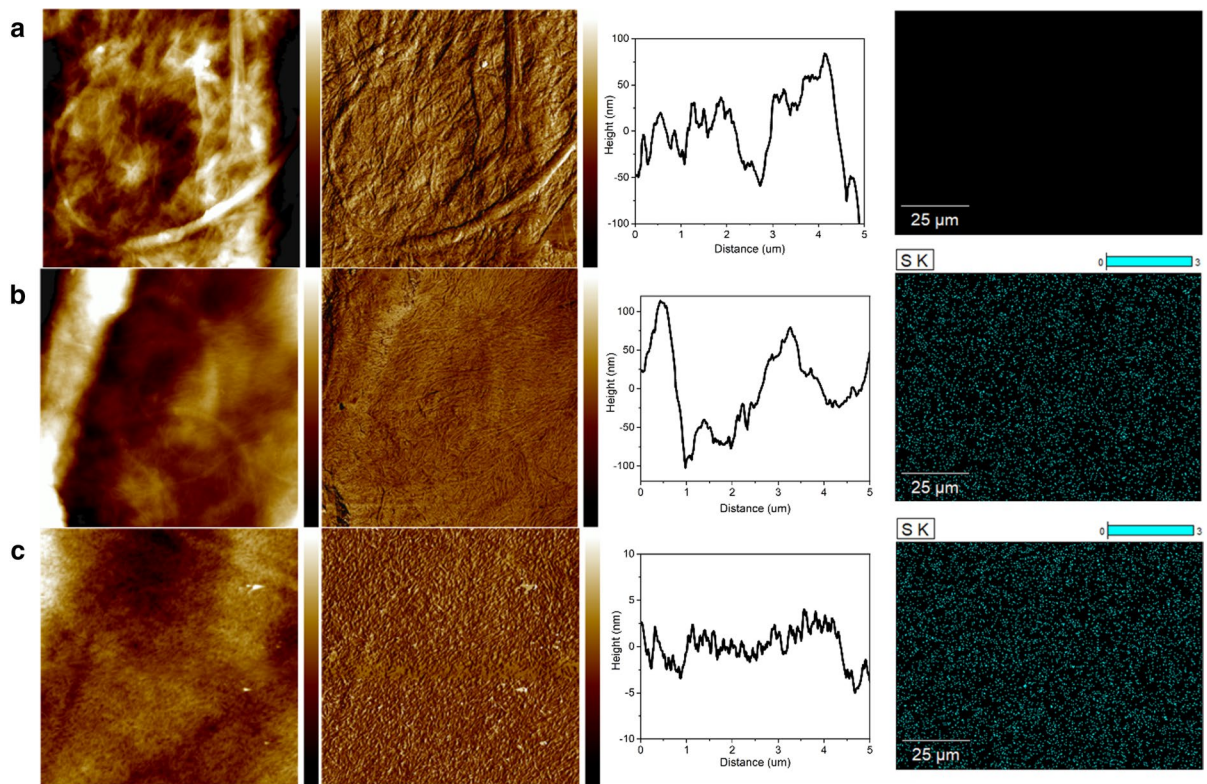
Fig. 3 AFM height (1st column) and phase (2nd column) images (5 μm × 5 μm) and their profiles (third column). Note the different height scales in the figures. **a** CNF100 + s (height bar ± 110 nm), **b** CNF50CNC50 + s (height bar ± 175 nm) and **c** CNC100 + s (height bar ± 30 nm). Spectral images (4th column) visualizing CNC distribution by detecting sulfur (S) by EDS. EDS data was collected with 1000 × magnification

is indicative to the sulfate ester group introduced to the surface of CNCs when prepared by sulfuric acid hydrolysis. The peaks around 2000–2250 cm^{-1} are assumed arise from CO_2 in air as the FTIR instrument is very sensitive towards it.

### Morphology of hybrid films by AFM and SEM

AFM and SEM images (Fig. 3; Suppl. Fig. S5) visualize the structures and give information on the topography and morphology of the prepared films. CNC100 + s film had a much smoother surface compared to the samples containing CNFs, the height variation of the CNF100 + s being almost 100-fold compared to CNC100 + s. CNF100 + s and CNF50CNC50 + s were imaged with 5 kV and

Table 2 Mechanical properties of CNF/CNC hybrid films

Sample	Tensile strength (MPa)	Young's modulus (GPa)	Strain at break (%)
CNF100	147 ± 33	5.9 ± 0.4	9.5 ± 4.5
CNF75CNC25	128 ± 18	7.1 ± 0.2	3.9 ± 1.6
CNF50CNC50	144 ± 12	6.6 ± 0.5	6.8 ± 1.7
CNF25CNC75	92 ± 7	7.4 ± 0.6	2.0 ± 0.4
CNC100	47 ± 14	5.2 ± 0.9	0.01 ± 0.005
CNF100 + s	85 ± 8	3.7 ± 0.7	6.9 ± 1.4
CNF-75CNC25 + s	89 ± 10	4.0 ± 0.3	9.1 ± 2.7
CNF-50CNC50 + s	72 ± 2	4.2 ± 0.1	11.25 ± 0.92
CNF-25CNC75 + s	43 ± 0.8	3.9 ± 0.2	6.6 ± 0.7
CNC100 + s	27 ± 0.7	2.0 ± 0.3	3.4 ± 0.3

CNC100 + s with 2 kV since it was easily destroyed with higher electron gun voltage. Due to the different size and shape of the nanocellulose materials, the films showed different morphologies in both AFM and SEM images. The smoother topography of CNC films observed in AFM height and phase images (Fig. 3c) suggest that CNCs form a denser film compared to the rougher and more porous network of CNFs (Figs. 1d, 3a). Hence, addition of CNCs may lead to denser films as suggested by the relatively smooth topography of the CNF50CNC50 + s sample (Fig. 3b). Energy-dispersive X-ray spectroscopy (EDS) was coupled with SEM to visualize the distribution of CNCs in the film. EDS detects the elemental sulfur originating from the sulfate groups on the CNC surface and confirmed the even distribution of CNCs in the films as no clear larger areas (black) without sulfur were detected (Fig. 3). As expected, sulfur was visible for CNF50CNC50 + s and CNC100 + s but not for CNF100 + s.

Mechanical properties

Table 2 presents the mechanical properties for CNF/CNC films with and without sorbitol. Tensile strength and elongation at break of all CNF/CNC hybrid films increased with increasing the ratio of CNFs. However, the correlation between the amount of CNFs and mechanical properties is not linear as the values for the films containing 50% of both CNFs and CNCs are much closer to CNF100 and

CNF100 + s films than the ones with only CNCs. This indicates that the CNF fibrillar structure also dominates the mechanical properties of the films, in addition to dominating the rheological properties. In addition to cellulose, it must be noted that the CNF dispersion also contains hemicelluloses, which is surrounding the fibrils. The hemicelluloses have been shown to have a significant strengthening effect when compared to CNF materials without hemicellulose (Kontturi et al. 2021). The hemicellulose at the surface of CNFs is suggested to increase the bonded area between fibrils. Addition of CNCs increased the stiffness of the film, which is seen as a slightly higher Young's modulus, but simultaneously elongation and tensile strength decreased to some extent. This is probably due to the densification of the film and higher degree of crystallinity. Addition of sorbitol improves the elongation at break for the samples containing CNCs but simultaneously decreases both tensile strength and Young's modulus, implying that sorbitol interrupts the formation of intermolecular hydrogen bonds within the nanocellulose films. These effects are characteristic for external plasticizers (Hubbe et al. 2017). For example, CNF100 showed the highest tensile strength 147 MPa, but it decreased to 85 MPa with the addition of sorbitol (CNF100 + s). The strength of pure CNF100 films; tensile strength 147 MPa, Young's modulus 5.9 GPa and strain at break 9.5%, are within the range of values previously reported for CNF films, although the values in literature vary
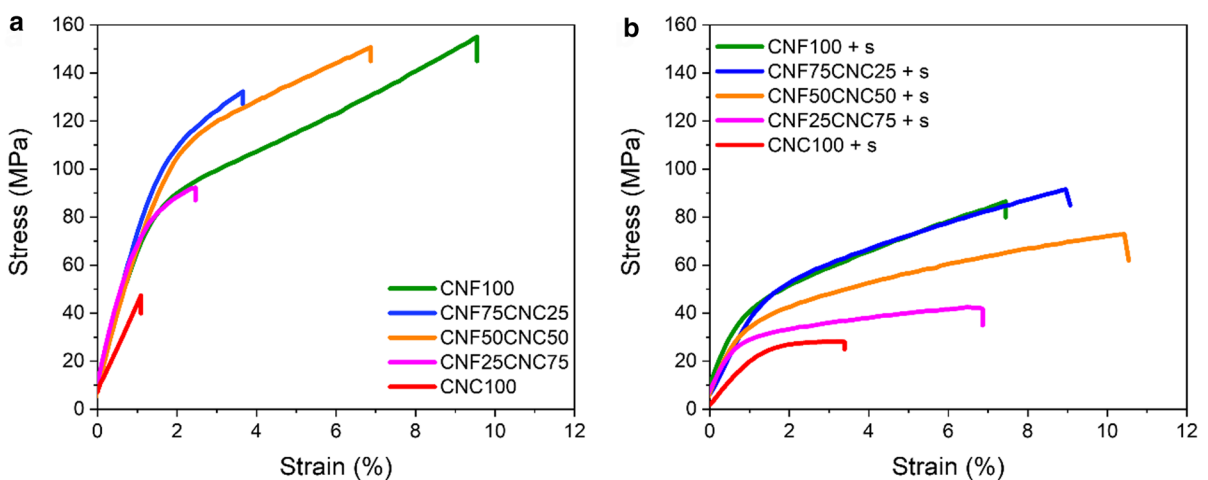
Fig. 4 Stress–strain curves of CNF/CNC hybrid films without sorbitol (**a**) and with sorbitol (**b**)

quite a lot depending on film preparation method, CNF raw material, and measuring parameters (Siró and Plackett 2010; Lee et al. 2014; Vartiainen et al. 2015). For example, CNF film prepared by vacuum filtration is densified due to pressure leading to films with higher strength properties (Österberg et al. 2013). The high elongation value is suspected to results from the shrinkage and wrinkling upon drying, which is known to affect also freely-dried papers (Kouko and Retulainen 2018). Thus, we prepared a 100% CNF film by solvent casting on a petri dish, which results in more even films. The elongation at break for this film was measured to be 5% (Suppl. Table S1), which shows that the shrinkage during the drying phase has an effect on the elongation value.

Typical stress–strain curves of CNF/CNC hybrid films with and without sorbitol presented in Fig. 4 provide further insight into the tensile behavior of the hybrid films. Of the pure CNF/CNC films without sorbitol, all films except CNC100 showed plastic region, the linear yield starting between 1–2% strain. The yield stress however varied between the samples. The linear yield for CNF25CNC75 was already quite short indicating that the mechanical performance of CNCs starts to dominate. The film formed of pure CNCs (CNC100) was not able to yield because the nanoparticle has a shape of a rigid rod, which does not allow entanglement. Addition of sorbitol to the CNC film (CNC100 + s) brought flexibility to the film enabling it to yield. Generally, yielding of the CNF network has been speculated to be associated with interfibrillar debonding and nanofibril slippage facilitated by voids, nanofibril bending and plasticity (Henriksson et al. 2008). Comparing Fig. 4a, b it can be noted that sorbitol was able to soften the nanocellulose films (increased strain) but at the same time it weakened the CNF network and interaction of nanocelluloses, which led to decreased strength and modulus.

Optical properties

We used an integrated sphere as well as an UV–Vis spectrometer to assess the optical properties of the hybrid films. Transmittance, forward and backward scattering, absorption and the forward scattering angle were measured using the integrated sphere (Fig. 5; Suppl. Fig. S6). Transmittance was measured in parallel using the UV–Vis spectrometer to evaluate the transparency of the samples (Suppl. Fig. S7). Based on the UV–Vis measurements the films formed from pure CNC suspensions (CNC100 and CNC100 + s) exhibited the highest optical transmittance. With the addition of CNFs to the film, the transmittance decreased gradually, being the lowest for CNF100 and

Fig. 5 **a** Transmittance and forward scattering (Haze) of CNF-CNC films with and without sorbitol (+S means with sorbitol). **b** Forward scattering angle. **c** Forward scattering images at 313 mm distance (+S means with sorbitol)
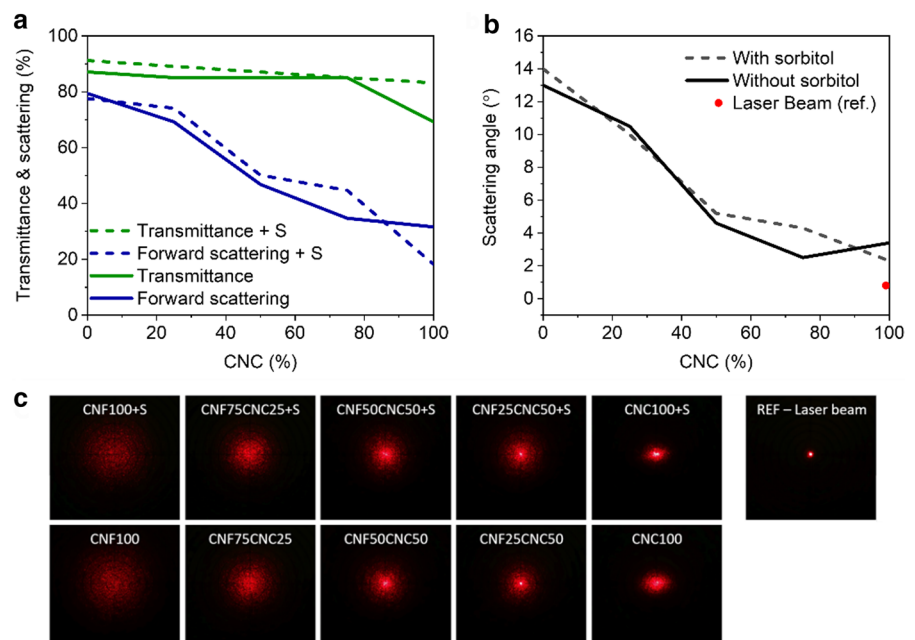
Table 3 Oxygen transmission rate (OTR) and oxygen permeability (OP) values for CNF/CNC + sorbitol films in 50% RH

Sample	Thickness (μm)	normalized OTR (cc*μm/m²*day)	OP (cc*μm/ m²*day*kPa)
CNF100 + s	33	62.3 ± 12	0.61 ± 0.12
CNF75CNC25 + s	34	51.4 ± 6	0.51 ± 0.06
CNF50CNC50 + s	48	66.9 ± 3	0.66 ± 0.03
CNF25CNC75 + s	43	86.4 ± 1	0.85 ± 0.01
CNC 100 + s	57	102 ± 7	1.04 ± 0.07

CNF100 + s. The result seems intuitive, as the pure CNC films appeared also visually most transparent. On the contrary, the results obtained with the integrated sphere showed that the transmittance remained around 80% and no clear decrease was observed with the addition of CNCs (Fig. 5a). Thus, the same amount of light was transmitted through all the films. However, the scattering of transmitted light and scattering angle decreased with the addition of CNCs (Fig. 5b, c) and similar behavior has been reported previously (Xu et al. 2016). The UV–Vis spectrometer does not collect scattered light well as it measures only the direct transmittance. This is why, for the UV–Vis results, the transmittance seems to decrease when the CNF concentration is increasing. The differences in the scattering of light for the hybrid films originate from fiber size, porosity and surface roughness (Zhu et al. 2013; Toivonen et al. 2018). As seen in Fig. 3, increasing the CNC amount led to decrease in surface roughness, while the lowest porosity was observed for the CNF50CNC50 sample. The relative transmittance spectrum as a function of the wavelength is still valid in the UV/Vis measurements (Suppl. Fig. S7), but the absolute transmittance value of each sample depends on the scattering. As the increased scattering of light causes the films to be opaquer, the transparency of the CNF/CNC hybrids films can simply be controlled by adjusting the ratio between the two components.

Barrier properties

Increasing the oxygen barrier properties of films used for example for food packaging is important since the penetrated oxygen is able oxidize the food products producing off-odors and flavors making them less appealing and even spoiled. The air permeance for all samples was at the lower detection limit (0.003 μm/

(Pa*s)) of the equipment indicating that the films were homogeneous without any big holes or connected pores. Hence, we also measured the oxygen transmission rate for the films containing sorbitol and the oxygen barrier for all samples was very good (Table 3). The pure CNF sample with sorbitol (CNF100 + s) had similar values as reported for CNF films earlier (Nair et al. 2014). The oxygen permeability decreased with a 25% increase in the CNC content. When the CNC content in the hybrid film reached 50%, the OTR value increased again, however remained close to the value of the 100% CNF film. Belbekhouche et al. (2011), report higher oxygen transmission for CNC films compared to CNF films. They explain the higher oxygen transmission for CNC films with difference in porosity as well as with the tortuosity of gas molecules to diffuse through an entangled network of CNFs. We suspect that a small increase in the CNC content fills the voids within the CNF/CNC hybrid film (i.e. decreases porosity, Fig. 1d) leading to decreased oxygen permeability. However, when the amount of CNCs in the hybrid film increases enough, in our case to 50%, the tortuosity of the diffusion pathway decreases, and it is easier for the oxygen molecules to permeate through the film. Our results showed that the oxygen permeability increased slightly even though the porosity value was the lowest for CNF50CNC50 + s film. This indicates a more pronounced role of the entangled network compared to the porosity. One well-known parameter affecting the O_2 diffusion is also crystallinity (McGonigle et al. 2001). Usually the higher the crystallinity the lower the gas diffusion. Even though CNCs have higher crystallinity values compared to CNFs (Rahimi Kord Sofla et al. 2016), the CNF films showed lower oxygen permeability due to the entangled network structure.

We measured the grease barrier properties for all films for a period of 7 days. During this time, no grease permeation through the film onto the blotting paper was visible, indicating that the films are resistant to olive oil. For normal paper (copy paper), the grease permeated already within 10 min and was visible on the blotting paper (Suppl. Fig. S8).

Preparation of a defined optical pattern on CNF50CNC50 + s film using controlled dissolution with NMMO

We demonstrated that it is possible to create defined millimeter size patterns on CNF/CNC hybrid films by
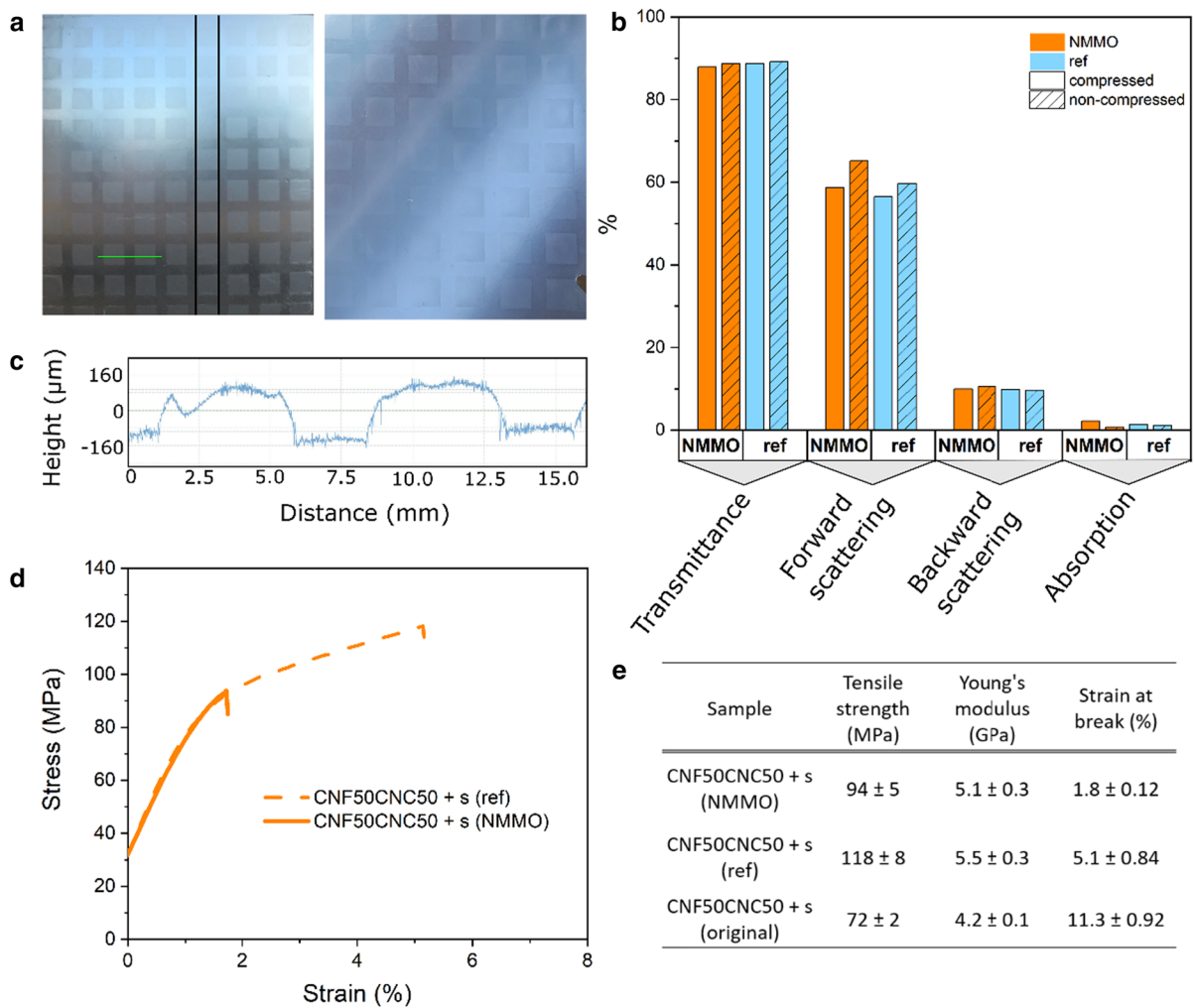
Fig. 6 a Film after preparation of a defined structure by controlled dissolution with NMMO applying heat and pressure (left), reference after only applying heat and pressure but no NMMO (right). The black lines indicate the size of the strip that was cut for the mechanical testing. **b** Optical properties of the patterned NMMO-treated film and reference film (without NMMO) measured from both compressed (between squares) and non-compressed areas (squares). **c** Confocal microscopy profile across 2 squares (green line in **a**). **d** Typical stress–strain curves of the strip of patterned NMMO-treated film and its reference sample. **e** Table of mechanical properties of the patterned films (NMMO and ref) and the original reference sample without patterning (original)

controlled dissolution using simultaneously NMMO, heat and compression with a metal grid. The process created a grid like pattern on the CNF50CNC50 + s films, which was seen as higher transparency in the compressed areas (Fig. 6a). The reference sample that was compressed without NMMO also showed increased transparency in the compressed areas, however visually the transparency appeared to be slightly lower. The increased transparency of the compressed areas in Fig. 6a for both the NMMO treated sample

and the reference that was compressed without the solvent result from the decreased surface roughness due to compression. The difference in transparency between compressed and non-compressed areas for the NMMO treated sample is more pronounced than for the reference sample as the partial dissolution of the film surface creates an even smoother surface compared to the reference. Optical properties were measured with the integrated sphere for both the NMMO treated film and the reference sample and

were determined for both the compressed (between squares) and non-compressed areas (squares) (Fig. 6b). Forward scattering i.e. haze decreased in the compressed areas (6.4%) for the NMMO treated sample and also contributed to the increased transparency in these areas as the denser, partially dissolved and regenerated areas, have fewer scattering interfaces. The difference between the areas is not as large for the reference sample that was compressed without NMMO (3.2%). The magnitude of forward scattering is mostly defined by the thickness of the sample. As the thickness is not assumed to drastically decrease due to the compression and partial dissolution also the differences in haze values remain small. The small difference in the decreased haze value between the NMMO treated (6%) and reference (3%), however, indicates that the NMMO treatment is able to create a slightly denser structure by partially dissolving the cellulose at the film surface. Confocal microscopy profiles (Fig. 6c) show the height variation of the patterned surface. The height difference between compressed and non-compressed areas was approximately 100 μm. The value is higher than the original film thickness (48 μm) as paper and cellophane were used in the compression leading to elongation of the film. To detect changes in crystallinity from more crystalline to amorphous in the CNF/CNC film after controlled dissolution, we used solid state ^{13}C NMR. In the NMR spectra (Suppl. Fig. S9) the peak at 84–89 ppm is assigned to the C4 carbon of ordered cellulose and the peak at 77–84 to the C4 carbon of disordered cellulose. The crystallinity was calculated by dividing the area of the crystalline peak (integral of peak 84–89 ppm) by the total area of the C4 peak (integrating the region from 77 to 89). The crystallinity decreased from 51 to 46% in both the NMMO treated and the reference sample from areas where pressure had been applied confirming higher degree of amorphous cellulose in the treated areas. As the changes are similar for both the NMMO treated sample and reference it suggests that only slight changes due to dissolution/regeneration appear on the surface of the films. The tensile properties of the strip, where compressed and non-compressed areas alternated in a sequential series were measured to see the effect of the patterning treatment. The tensile strength increased in both the NMMO treated and reference sample compared to the original CNF50CNC50 + s film (Fig. 6d, e). We hypothesize that the combination

of heat and mechanical compression condenses the film, forming a denser structure and thus increases the intermolecular bonding of the nanocelluloses. Similar effect on tensile strength has been reported previously by applying heat and mechanical compression on CNF films (Österberg et al. 2013). However, it is important to note that the measured sample is very different due to the repeating structure of compressed and non-compressed areas, which has an influence on the mechanical performance. The tensile strength and Young's modulus after heating and compression were higher for the reference sample (118 ± 8 MPa and 5.3 ± 0.3 GPa) than the NMMO treated sample (94 ± 5 MPa and 5.1 ± 0.3 GPa). The strain decreased for both samples and more drastically for the NMMO treated. This is in contrast with the observations of Orelma et al. (2017). They found that partial dissolution with NMMO decreased the strain of the CNF film making it more rigid.

Conclusion

Nanocellulose hybrid films were prepared by combining cellulose nanofibrils and cellulose nanocrystals. We found that the properties varied depending on the ratio between CNFs and CNCs in the film. Surface roughness and porosity decreased with an increase in the CNC content providing smoother and denser films up to 50% CNCs. The films containing 50% of both CNFs and CNCs showed excellent mechanical properties, where the CNFs were dominating the behavior bringing both strength and flexibility to the film. Addition of sorbitol decreased the strength but made the films more uniform and flexible. By increasing the CNC content of the hybrid film, transparency of the films could be increased due to lowered scattering. Addition of a small amount (up to 25%) of CNCs enhanced the oxygen barrier of the films and the barrier was remained at the same level as for 100% CNF film even with the addition of 50% CNCs. In addition, all films showed excellent barrier properties against grease. Finally, we demonstrated the fabrication of specific patterning on the hybrid films by the controlled dissolution process, which further tunes the optical and mechanical properties of the films. Hybrid films prepared in this study could be potentially used for example in packaging applications.

Declarations

Conflict of interest The authors declare no conflicts of interest.

References

Aulin C, Gällstedt M, Lindström T (2010) Oxygen and oil barrier properties of microfibrillated cellulose films and coatings. Cellulose 17:559–574. https://doi.org/10.1007/s10570-009-9393-y

Belbekhouche S, Bras J, Siqueira G et al (2011) Water sorption behavior and gas barrier properties of cellulose whiskers and microfibrils films. Carbohydr Polym 83:1740–1748. https://doi.org/10.1016/j.carbpol.2010.10.036

Chen G, Zhang B, Zhao J, Chen H (2013) Improved process for the production of cellulose sulfate using sulfuric acid/ethanol solution. Carbohydr Polym 95:332–337. https://doi.org/10.1016/j.carbpol.2013.03.003

Chen F, Sawada D, Hummel M et al (2020) Unidirectional all-cellulose composites from flax via controlled impregnation with ionic liquid. Polymer. https://doi.org/10.3390/polym12051010

De France KJ, Hoare T, Cranston ED (2017) Review of hydrogels and aerogels containing nanocellulose. Chem Mater 29:4609–4631. https://doi.org/10.1021/acs.chemmater.7b00531

Fan M, Dai D, Huang B (2012) Fourier transform infrared spectroscopy for natural fibres. In: Salih S (ed) Fourier transform: materials analysis. InTech, Rijeka, pp 45–69

Hansen NML, Blomfeldt TOJ, Hedenqvist MS, Plackett DV (2012) Properties of plasticized composite films prepared from nanofibrillated cellulose and birch wood xylan. Cellulose 19:2015–2031. https://doi.org/10.1007/s10570-012-9764-7

Henriksson M, Berglund LA, Isaksson P et al (2008) Cellulose nanopaper structures of high toughness. Biomacromol 9:1579–1585. https://doi.org/10.1021/bm800038n

Herrera MA, Mathew AP, Oksman K (2014) Gas permeability and selectivity of cellulose nanocrystals films (layers) deposited by spin coating. Carbohydr Polym 112:494–501. https://doi.org/10.1016/j.carbpol.2014.06.036

Hubbe MA, Ferrer A, Tyagi P et al (2017) Nanocellulose in thin films, coatings, and plies for packaging applications: a review. BioResources 12:2143–2233

Klemm D, Philipp B, Heinze T, Heinze U, Wagenknecht W (1998) Comprehensive cellulose chemistry. Fundamentals and analytical methods, vol 1. Wiley-VCH Verlag GmbH, Weinheim

Klemm D, Heublein B, Fink H-P, Bohn A (2005) Cellulose: fascinating biopolymer and sustainable raw material. Angew Chemie Int Ed 44:3358–3393. https://doi.org/10.1002/anie.200460587

Klemm D, Kramer F, Moritz S et al (2011) Nanocelluloses: a new family of nature-based materials. Angew Chemie Int Ed 50:5438–5466. https://doi.org/10.1002/anie.201001273

Kontturi KS, Lee KY, Jones MP et al (2021) Influence of biological origin on the tensile properties of cellulose nanopapers. Cellulose 28:6619–6628. https://doi.org/10.1007/S10570-021-03935-2/FIGURES/5

Koppolu R, Abitbol T, Kumar V et al (2018) Continuous roll-to-roll coating of cellulose nanocrystals onto paperboard.

Cellulose 25:6055–6069. https://doi.org/10.1007/s10570-018-1958-1

Kouko J, Retulainen E (2018) The relationship between shrinkage and elongation of bleached softwood kraft pulp sheets. Nord Pulp Pap Res J 33:522–533. https://doi.org/10.1515/NPPRJ-2018-3057

Lavoine N, Bergström L (2017) Nanocellulose-based foams and aerogels: processing, properties, and applications. J Mater Chem A 5:16105–16117

Lee KY, Aitomäki Y, Berglund LA et al (2014) On the use of nanocellulose as reinforcement in polymer matrix composites. Compos Sci Technol 105:15–27

Li J, Nawaz H, Wu J et al (2018) All-cellulose composites based on the self-reinforced effect. Compos Commun 9:42–53. https://doi.org/10.1016/j.coco.2018.04.008

Liu D, Chen X, Yue Y et al (2011) Structure and rheology of nanocrystalline cellulose. Carbohydr Polym 84:316–322. https://doi.org/10.1016/j.carbpol.2010.11.039

Lundahl MJ, Klar V, Wang L et al (2017) Spinning of cellulose nanofibrils into filaments: a review. Ind Eng Chem Res 56:8–19

Ma H, Zhou B, Li HS et al (2011) Green composite films composed of nanocrystalline cellulose and a cellulose matrix regenerated from functionalized ionic liquid solution. Carbohydr Polym 84:383–389. https://doi.org/10.1016/j.carbpol.2010.11.050

McGonigle EA, Liggat JJ, Pethrick RA et al (2001) Permeability of N2, Ar, He, O2 and CO2 through biaxially oriented polyester films: dependence on free volume. Polymer (Guildf) 42:2413–2426. https://doi.org/10.1016/S0032-3861(00)00615-7

Nair SS, Zhu J, Deng Y, Ragauskas AJ (2014) High performance green barriers based on nanocellulose. Sustain Chem Process 2:1–7. https://doi.org/10.1186/s40508-014-0023-0

Nishino T, Matsuda I, Hirao K (2004) All-cellulose composite. Macromolecules 37:7683–7687. https://doi.org/10.1021/ma049300h

Onogi S, Asada T (1980) Rheology and rheo-optics of polymer liquid crystals. Astarita g, Marrucci g, Nicolais L. Proc Eighth Int Congr Rheol Plenum Napoles 1:126–136. https://doi.org/10.1007/978-1-4684-3740-9_9

Orelma H, Korpela A, Kunnari V et al (2017) Improving the mechanical properties of CNF films by NMMO partial dissolution with hot calender activation. Cellulose 24:1691–1704. https://doi.org/10.1007/s10570-017-1229-6

Österberg M, Vartiainen J, Lucenius J et al (2013) A fast method to produce strong NFC films as a platform for barrier and functional materials. ACS Appl Mater Interfaces 5:4640–4647. https://doi.org/10.1021/am401046x

Pääkko M, Ankerfors M, Kosonen H et al (2007) Enzymatic hydrolysis combined with mechanical shearing and high-pressure homogenization for nanoscale cellulose fibrils and strong gels. Biomacromol 8:1934–1941. https://doi.org/10.1021/bm061215p

Plackett D, Anturi H, Hedenqvist M et al (2010) Physical properties and morphology of films prepared from microfibrillated cellulose and microfibrillated cellulose in combination with amylopectin. J Appl Polym Sci n/a-n/a. https://doi.org/10.1002/app.32254

Rahimi Kord Sofla M, Brown RJ, Tsuzuki T, Rainey TJ (2016) A comparison of cellulose nanocrystals and cellulose nanofibres extracted from bagasse using acid and ball milling methods. Adv Nat Sci Nanosci Nanotechnol. https://doi.org/10.1088/2043-6262/7/3/035004

Revol JF, Bradford H, Giasson J et al (1992) Helicoidal self-ordering of cellulose microfibrils in aqueous suspension. Int J Biol Macromol 14:170–172. https://doi.org/10.1016/S0141-8130(05)80008-X

Saleh BEA, Teich MC (1991) Fundamentals of photonics. Wiley, New York. https://doi.org/10.1002/0471213748

Sathre R, Gustavsson L (2009) Using wood products to mitigate climate change: external costs and structural change. Appl Energy 86:251–257. https://doi.org/10.1016/j.apenergy.2008.04.007

Saxena A, Elder TJ, Kenvin J, Ragauskas AJ (2010) High oxygen nanocomposite barrier films based on Xylan and nanocrystalline cellulose. Nano-Micro Lett 2:235–241. https://doi.org/10.1007/bf03353849

Shafeiei-Sabet S, Hamad WY, Hatzikiriakos SG (2013) Influence of degree of sulfation on the rheology of cellulose nanocrystal suspensions. Rheol Acta 52:741–751. https://doi.org/10.1007/s00397-013-0722-6

Shafiei-Sabet S, Hamad WY, Hatzikiriakos SG (2012) Rheology of nanocrystalline cellulose aqueous suspensions. Langmuir 28:17124–17133. https://doi.org/10.1021/la303380v

Siró I, Plackett D (2010) Microfibrillated cellulose and new nanocomposite materials: a review. Cellulose 17:459–494

Sun X, Wu Q, Ren S, Lei T (2015) Comparison of highly transparent all-cellulose nanopaper prepared using sulfuric acid and TEMPO-mediated oxidation methods. Cellulose 22:1123–1133. https://doi.org/10.1007/s10570-015-0574-6

Syverud K, Stenius P (2009) Strength and barrier properties of MFC films. Cellulose 16:75–85. https://doi.org/10.1007/s10570-008-9244-2

Toivonen MS, Onelli OD, Jacucci G et al (2018) Anomalous-diffusion-assisted brightness in white cellulose nanofibril membranes. Adv Mater 30:1704050. https://doi.org/10.1002/ADMA.201704050

Ureña-Benavides EE, Ao G, Davis VA, Kitchens CL (2011) Rheology and phase behavior of lyotropic cellulose nanocrystal suspensions. Macromolecules 44:8990–8998. https://doi.org/10.1021/ma201649f

Vähä-Nissi M, Laine C, Rautkoski H et al (2016) Test methods for evaluating grease and mineral oil barriers

Vartiainen J, Lahtinen P, Kaljunen T, Kunnari V, Peresin MS, Tammelin T (2015) Comparison of properties between cellulose nanofibrils made from banana, sugar beet, hemp, softwood and hardwood pulps. O Pap 76(3):1

Xu X, Liu F, Jiang L et al (2013) Cellulose nanocrystals vs. cellulose nanofibrils: a comparative study on their microstructures and effects as polymer reinforcing agents. ACS Appl Mater Interfaces 5:2999–3009. https://doi.org/10.1021/am302624t

Xu X, Zhou J, Jiang L et al (2016) Highly transparent, low-haze, hybrid cellulose nanopaper as electrodes for flexible electronics. Nanoscale 8:12294–12306. https://doi.org/10.1039/c6nr02245f

Yang Q, Saito T, Berglund LA, Isogai A (2015) Cellulose nanofibrils improve the properties of all-cellulose composites by the nano-reinforcement mechanism and nanofibril-induced crystallization. Nanoscale 7:17957–17963. https://doi.org/10.1039/c5nr05511c

Zhao J, He X, Wang Y et al (2014) Reinforcement of all-cellulose nanocomposite films using native cellulose nanofibrils. Carbohydr Polym 104:143–150. https://doi.org/10.1016/j.carbpol.2014.01.007

Zhu H, Parvinian S, Preston C et al (2013) Transparent nanopaper with tailored optical properties. Nanoscale 5:3787–3792. https://doi.org/10.1039/c3nr00520h